



## Full length article

## The role of lattice defects, element partitioning and intrinsic heat effects on the microstructure in selective laser melted Ti-6Al-4V



Jan Haubrich<sup>a,\*</sup>, Joachim Gussone<sup>a</sup>, Pere Barriobero-Vila<sup>a</sup>, Philipp Kürnsteiner<sup>b</sup>, Eric A. Jäggle<sup>b</sup>, Dierk Raabe<sup>b</sup>, Norbert Schell<sup>c</sup>, Guillermo Requena<sup>a,d</sup>

<sup>a</sup> Institute of Materials Research, German Aerospace Center (DLR), Linder Höhe, Cologne, 51147, Germany

<sup>b</sup> Max-Planck-Institut für Eisenforschung GmbH, Department Microstruct. Physics and Alloy Design, Max-Planck-Str. 1, 40237, Duesseldorf, Germany

<sup>c</sup> Institute of Materials Research, Helmholtz-Zentrum Geesthacht, Max-Planck-Str. 1, 21502, Geesthacht, Germany

<sup>d</sup> Metallic Structures and Materials Systems for Aerospace Engineering, RWTH Aachen University, Aachen, 52062, Germany

## ARTICLE INFO

## Article history:

Received 6 December 2018

Received in revised form

23 January 2019

Accepted 24 January 2019

Available online 30 January 2019

## Keywords:

Selective laser melting

Titanium alloys

Martensite decomposition

High energy synchrotron X-ray diffraction

Atom-probe tomography

## ABSTRACT

The microstructure and phase composition in selective laser melted (SLM) Ti-6Al-4V plays a key role for its mechanical performance. The microstructure evolution in SLM Ti-6Al-4V was studied in the as-built condition and after sub-transus heat treatments between 400 °C and 800 °C focusing on elemental partitioning and the role of lattice defects on precipitation of the  $\beta$  phase. With SLM parameters corresponding to low volume energy density ( $E_V = 77 \text{ J/mm}^3$ ) the as-built microstructure consisted of acicular martensite and showed a higher density of lattice defects than that synthesized under high  $E_V = 145 \text{ J/mm}^3$  condition. High energy X-ray synchrotron diffraction indicated the presence of  $\sim 2 \text{ wt.}\%$   $\beta$ -phase at this high  $E_V$ . Moreover, atom-probe tomography revealed enrichments in  $\beta$ -stabilizers at one- and two-dimensional lattice defects. These fine enriched one-dimensional columnar and two-dimensional features are identified as precursors of  $\beta$ -phase, revealing the role of lattice defects for  $\beta$ -precipitation. Upon annealing at 400 °C and 530 °C,  $\beta$ -films began to fragment into  $\beta$ -platelets and nanoparticles, whereas annealing at 800 °C led to a coarse-lamellar  $\alpha/\beta$ -microstructure. Moreover,  $\alpha_2$ -Ti<sub>3</sub>Al was found in the 400 °C annealed condition. In line with the microstructure changes, Vickers hardness increased upon annealing at temperatures up to 530 °C and dropped when coarsening occurred at higher temperatures. Substantial element partitioning occurred during thermally driven martensite decomposition, which was significantly stronger for Fe than for V.

© 2019 Acta Materialia Inc. Published by Elsevier Ltd. All rights reserved.

## 1. Introduction

Laser-based additive manufacturing (AM) is of interest since it opens an opportunity of near net-shape manufacturing of metallic components. In particular, its inherent high design freedom enables complex-shaped parts that are difficult or impossible to realize by conventional manufacturing methods. AM is often considered to represent a disruptive technology that may revolutionize the industrial manufacturing of metallic structures [1–3]. Yet, AM processing and manufacturing chains, and particularly the required materials suited for AM are still in their infancy when targeting

safety-critical structural applications.

Ti-6Al-4V (wt.%), the most used and studied titanium alloy for AM, has high specific strength, low mass density and high corrosion resistance up to 350 °C [4]. It is by far the most successful Ti alloy commercially applied as wrought or cast product (>50% of the global market of titanium alloys) and is used e.g. in various aerospace applications [4,5].

Typically, selective laser melting (SLM) of Ti-6Al-4V under processing conditions optimized for low residual porosity results in reduced ductility, owing to a mainly martensitic microstructure (e.g. [6–15]) as a consequence of the fast cooling rates (reported between  $\sim 10^3 - 10^8 \text{ K/s}$ ) during SLM [8,16–19]. These microstructures consist of fine acicular  $\alpha'$  martensite [8,10–12,20–22] formed within columnar prior  $\beta$ -grains. These prior  $\beta$ -grains grow epitaxially along  $\beta$ -(100) in the build direction due to directional cooling, which lends the SLM materials a strong crystallographic texture [3,6,13,14,23]. Moreover, the fine  $\alpha'$  martensite can contain a high

\* Corresponding author.

E-mail addresses: [jan.haubrich@dlr.de](mailto:jan.haubrich@dlr.de) (J. Haubrich), [joachim.gussone@dlr.de](mailto:joachim.gussone@dlr.de) (J. Gussone), [pere.barrioberovila@dlr.de](mailto:pere.barrioberovila@dlr.de) (P. Barriobero-Vila), [p.kuernsteiner@mpie.de](mailto:p.kuernsteiner@mpie.de) (P. Kürnsteiner), [e.jaegle@mpie.de](mailto:e.jaegle@mpie.de) (E.A. Jäggle), [d.raabe@mpie.de](mailto:d.raabe@mpie.de) (D. Raabe), [norbert.schell@hzg.de](mailto:norbert.schell@hzg.de) (N. Schell), [guillermo.requena@dlr.de](mailto:guillermo.requena@dlr.de) (G. Requena).

density of crystallographic defects such as twin boundaries, dislocations and stacking faults [11–13,22,24].

The heat supplied by the laser beam “intrinsically” during the build-up process allows adjusting the resulting as-built microstructures by varying the introduced energy density. This is a consequence of the energy applied by the track-wise and layer-wise laser processing inherent to SLM, which is often termed “intrinsic heat treatment” (IHT) [3,9–11,25,26]. The SLM parameters can be adjusted for martensite decomposition by reducing the hatch distance or the scan velocity, both of which reduce the build rate substantially. An “intensified IHT” can be achieved that allows to partially or even largely stabilize  $\alpha/\beta$  microstructures with fine lamellar  $\alpha$  laths [3,9–11,20] and leads to graded microstructures along the build direction with a reduced crystallographic texture [3,20]. A prerequisite for achieving the effects of an intensified IHT is to have sufficiently short layer processing times, so that the cooldown of the part being built is limited before the next layer and thus the next heat input is added.

The most common approaches to adjust the microstructure, decomposition of martensite and reducing residual stress in ALM Ti-6Al-4V consist of ex situ post-heat treatments and hot isostatic pressing. Since a single step annealing above the  $\beta$ -transus temperature followed by slow cooling has a detrimental effect on ultimate tensile strength [8,27] due to rapid coarsening of  $\beta$ , subtransus treatments are of particular interest.

A subtransus treatment allows for a thermally activated, diffusion-controlled decomposition of  $\alpha'$  martensite, resulting in a partially or fully stabilized lamellar  $\alpha/\beta$  microstructure [8,13,22,27–29]. Coarsening of  $\alpha$  plates takes place upon increasing the annealing temperatures, resulting in a decrease of strength and hardness following a Hall-Petch relationship [8,22,27–29]. Micro-analytical studies of IHT effects on Ti-6Al-4V show that the rejection of V from the  $\alpha'$  martensite during its decomposition results in the precipitation of  $\beta$  at martensite plate boundaries, while it has even been proposed that lattice defects such as stacking faults and twin boundaries play a role in the process of formation of  $\beta$  although a detailed systematic analysis is still missing [3,30]. This also suggests that the large amount of crystallographic defects usually found within martensite plates in as-built Ti-6Al-4V processed by SLM may be exploited as nucleation sites for  $\beta$  in order to obtain acceptable strength-ductility trade-offs for AM. Therefore, in this study we apply micro- and nano-analytical analyses to reveal element partitioning and the role of lattice defects in the process of formation of  $\beta$  during martensite decomposition by IHT and during sub-transus annealing treatments.

## 2. Experimental

### 2.1. Selective laser melting

Cubic samples with a size of  $10 \times 10 \times 10 \text{ mm}^3$  were produced on an SLM Solutions 280 HL machine using Ti-6Al-4V ELI (grade 23) alloy powder in an argon 5.0 atm at a constant building platform temperature of 200 °C. The powder that was produced by means of plasma atomization was purchased from Advanced Powders & Coatings (AP&C), Canada. The size distribution of the powder's spherical particles was measured by laser diffraction (Beckman Coulter LS 13320 PIDS), resulting in D-values  $D_{10} = 22 \mu\text{m}$ ,  $D_{50} = 34 \mu\text{m}$  and  $D_{90} = 46 \mu\text{m}$ . The chemical composition of the powder according to the specification provided by AP&C is 0.11 wt.% O (0.31 at.%), 6.4 wt.% Al (10.8 at.%), 4.0 wt.% V (3.6 at.%), and 0.20 wt.% Fe (0.16 at.%). Oxygen was determined by the powder provider AP&C using inert gas fusion following ASTM E1409 and the metallic elements were determined according to ASTM E2371 by direct current plasma emission spectroscopy.

All cubes were built in a single SLM build job on 2 mm high supports using the meandering “zig-zag” scanning strategy (layer to layer increment of 90°) [7]. Thus, any microstructure variations that might arise from differing sample geometries, size effects or changing layer building times were avoided. The build time per layer (exposure time plus coating time) was constant at 140 s. All samples for microanalysis were prepared from the central region of the cubes.

The determination of a processing window with optimized material density, i.e. minimized porosity, was carried out by defining sample parameters based on three different experimental strategies (Table 1): first, a *One factor at a time* (OFAT) variation of the scan velocity, and, subsequently, two *Design of Experiment* (DoE) full factorial parameter variations associated with high and low volume energy densities ( $E_v$ ) were carried out. The technical details defining these parameter ranges are explained in Table 1.

### 2.2. Heat treatments

The samples of the two SLM parameter combinations corresponding to the lower and upper volume energy density limits within the process window were chosen for analysis of the microstructural transformations. Heat treatments were carried out under high vacuum ( $<10^{-5}$  mbar) at temperatures,  $T = 400, 530, 650$  and  $800$  °C. The specimens were heated from room temperature (RT) with a heating rate of 10 K/min. Cooling rates between  $\sim 10$ – $50$  K/min were recorded during furnace cooling.

### 2.3. Characterization of the SLM material conditions

#### 2.3.1. Porosity measurements by the Archimedes method

The porosity of each as-built SLM Ti-6Al-4V cuboid (total = 118 cubes) was characterized by density measurements using the Archimedes principle. The sample density was determined using a precision balance (KERN ABT 120-5DM) equipped with a density determination kit (KERN YDB-03). A theoretical reference value for the mass density,  $\rho_{\text{theo}} = 4.424 \text{ g/cm}^3$ , was determined by comparing the results with those derived from 2D image evaluation (20 samples with 3 images each  $10 \times 10 \text{ mm}^2$  in size were evaluated) assuming that different SLM processing conditions neither affect the chemical composition nor the bulk density of the alloy significantly.

#### 2.3.2. Scanning electron microscopy

Scanning electron microscopy (SEM) was carried out in back-scattered electron mode (BSE) using a FEI Helios Nanolab 600i dual beam (electron and  $\text{Ga}^+$ ) microscope with a Circular backscatter detector (CBS). The samples were previously ground and polished using a 3- $\mu\text{m}$  diamond suspension and  $\text{SiO}_2\text{-H}_2\text{O-H}_2\text{O}_2$ .

#### 2.3.3. High-energy X-ray diffraction

High energy X-ray diffraction (HEXRD) experiments were performed at the beamline P07-HEMS at PETRA III (Deutsches Elektronen-Synchrotron, DESY, Hamburg, Germany) [31]. All measurements were carried out in transmission mode using a beam energy of 100 keV. The main experimental parameters of the HEXRD setup are summarized in Table 2. The instrumental calibration was obtained using  $\text{LaB}_6$  powder standard.

Patterns of entire Debye–Scherrer rings from the bulk Ti-6Al-4V SLM alloy were acquired. Samples of  $4 \times 4 \times 10 \text{ mm}^3$  (thickness = 4 mm) were investigated and kept fixed during acquisition. Azimuthal integration of the diffraction images for a  $2\theta$  range between 2.0 and 7.0° was carried out using the software Fit2D [32].

Rietveld analysis using the software TOPAS [33] provided quantitative evaluation of phase fractions and lattice parameters.

**Table 1**  
Main SLM processing parameters of test series carried out in this work.

Sample	$P$ Laser power [W]	$v$ Scanning velocity [mm/s]	$h$ Hatch distance [ $\mu\text{m}$ ]	$F$ Focal offset distance [mm]	$E_v^a$ Volume energy density [ $\text{J}/\text{mm}^3$ ]
OFAT	175	200–1000	100	2.0	53–292
DoE (high $E_v$ )	155, 165, 175	575, 600, 675	70, 85, 100	1.0, 2.0	77–145
DoE (low $E_v$ )	80, 100, 120	365, 465, 565	100, 120, 140	1.0, 2.0	34–110

$$^a E_v = \frac{P}{v \cdot h \cdot d} [\text{J}/\text{mm}^3]; \text{ layer thickness } d = 30 \mu\text{m}.$$

**Table 2**  
Main experimental parameters of the HEXRD experiments.

Energy [keV]	Wavelength [ $\text{\AA}$ ]	Slit-Aperture Size [ $\text{mm}^2$ ]	Sample-Detector Distance [mm]	Acquisition time [s]	Detector
100	0.124	$1 \times 1$	1601.2	2–3	Perkin Elmer XRD 1621

Moreover, the full width at half maximum (FWHM) of selected peaks was determined by single peak fitting using a Pseudo-Voigt peak approximation.

### 2.3.4. Atom-probe tomography

Atom Probe Tomography (APT) was used to reveal the presence and chemical composition of nanometre-sized elemental segregations and precipitates. Needle-shaped APT specimens were prepared by the standard lift-out technique [34,35] using a FEI Helios Nano-Lab 600i Focused Ion Beam (FIB)/Scanning Electron Microscopy (SEM) dual beam system. The specimens were sharpened by annular milling at 30 kV acceleration voltage and currents ranging from 0.23 nA (for the largest milling pattern) to 40 pA (for the smallest pattern). Finally a low-kV cleaning step at 5 kV was used to minimize Ga contaminations at the surface.

A Cameca local electrode atom probe (LEAP) 5000XS was used in this study for the APT investigations. The specimens were analysed at a base temperature of 70–80 K in laser mode using a laser energy of 40–60 pJ, a pulse rate of 500–833 kHz and a detection rate of 1.5–3%. Large datasets of 60–600 million ions per tip were acquired in this way. One single APT needle was probed in voltage mode at a base temperature of 80 K, pulse fraction of 15% of the applied voltage, pulse rate of 200 kHz and detection rate of 1.5% as reference measurement. The voltage and the laser mode measurements yielded the same chemical compositions within a narrow range.

The acquired APT data was reconstructed and analysed with the commercial software IVAS version 3.6.14 by CAMECA instruments. 3D grid based analysis was conducted using a grid spacing of 1 nm and a delocalization of 2 nm.

### 2.3.5. Vickers hardness

Vickers micro-hardness measurements of the mirror-polished, unetched sections parallel to the building direction of Ti-6Al SLM samples were performed using a Clemex MMT-X7 tester with an indentation weight of 200 g (HV 0.2) according to DIN EN ISO 6507. This resulted in indentations of  $\sim 30 \mu\text{m}$  diagonal length, which were considerably larger than the microstructural features within prior- $\beta$  grains. 100 data points were recorded along the building direction for each condition.

## 3. Results

### 3.1. Processing window

A two-stage strategy was chosen to define the SLM process

window. In the first step, a coarse processing parameter window was determined using an OFAT approach by evaluating the resulting material density of the bulk samples (minimization of porosity). In a second step, the processing window was refined using a parameter variation set up by DoE. The total porosity volume fraction measured for a wide range of SLM parameters (Table 1) by using the Archimedes method is plotted against the volume energy density ( $E_v$ ) in Fig. 1. Note that different parameter combinations can lead to different porosities, even though they have the same  $E_v$ . SLM parameter combinations falling in the range between  $\sim 70$  and  $\sim 150 \text{ J}/\text{mm}^3$  define a region of sufficiently low porosities of  $\sim 0.25 \text{ vol.}\%$ . A lower and an upper  $E_v$  limit of this region was subsequently selected to study the microstructure of the as-built bulk samples and their evolution upon post heat treatments:  $E_v = 77 \text{ J}/\text{mm}^3$  and  $145 \text{ J}/\text{mm}^3$  (see Fig. 1 and Table 3). The former SLM parameter set will lead to a weaker intrinsic heat input (treatment) to the material than the latter high  $E_v$  condition.

### 3.2. SLM as-built microstructures

The SLM as-built microstructures of the samples synthesized at  $E_v = 77$  and  $145 \text{ J}/\text{mm}^3$  show the presence of acicular  $\alpha'$  martensite distributed within prior  $\beta$  grains (Fig. 2 (a) and (d)). The contrast in the SEM-BSE images stems partially from electron channelling [36]

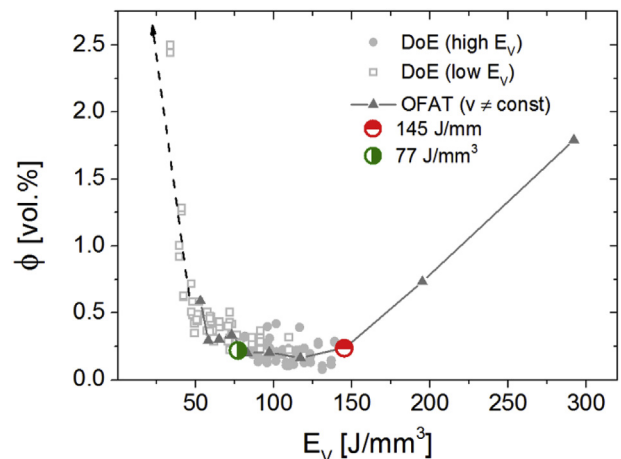


**Fig. 1.** Porosity volume fraction  $\phi$  of Ti-6Al-4V SLM samples as a function of volume energy density  $E_v$ .

**Table 3**  
SLM processing parameters of the samples selected for heat treatments and microstructural analysis.

Sample	$P$	$v$	$h$	$F$	$x$	$E_v$	Laser pattern strategy	Building platform temperature [°C]
	Laser power [W]	Scanning velocity [mm/s]	Hatch distance [ $\mu\text{m}$ ]	Focal offset distance [mm]	Layer thickness [ $\mu\text{m}$ ]	Volume energy density [ $\text{J}/\text{mm}^3$ ]		
H	175	575	70	1.0	30	145	Zig-zag scanning	200
L	155	675	100	1.0	30	77	Zig-zag scanning	200

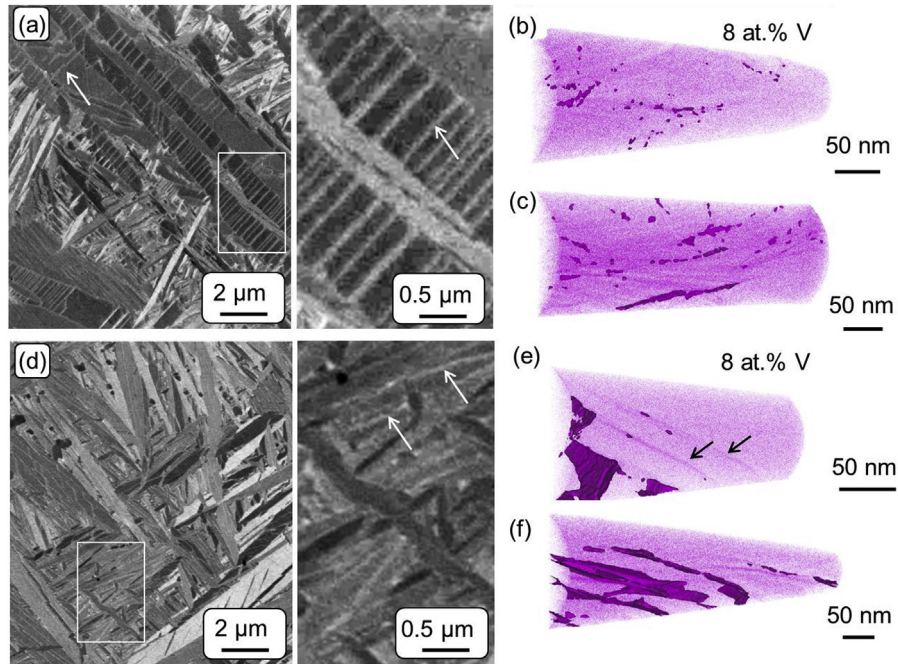


**Fig. 2.** SEM-BSE images and magnified regions of the as-built microstructure: (a)  $E_v = 77 \text{ J}/\text{mm}^3$  and (d)  $E_v = 145 \text{ J}/\text{mm}^3$ . Dark and mid-grey regions correspond to the  $\alpha'/\alpha$  matrix. The white arrows mark lattice defects in (a) and  $\beta$ -films in (d). The white boxes show the area of the magnified insets on the right side. Corresponding APT reconstructions for (b–c)  $E_v = 77 \text{ J}/\text{mm}^3$  (e–f) and  $145 \text{ J}/\text{mm}^3$ . The  $\beta$ -films are clearly recognized from the 8 at.% V iso-concentration surfaces in (e)–(f); examples of less V-enriched two-dimensional precursors are marked with arrows. Note that the APT measurement in (e) was acquired using the voltage mode.

and allows detecting a high density of lattice defects either within  $\alpha'$  or fragmenting the  $\alpha'$  laths such as stacking faults, dislocations and twin boundaries (one of these defects is marked by an arrow on the right side of Fig. 2 (a)). Such a high density of lattice defects are known for Ti-6Al-4V processed by AM methods with high cooling rates [11–13,22,24] and points to high internal stresses generated during cooling as previously proposed to account for the poor ductility shown by this alloy in this condition [12,13]. The microstructure obtained at higher  $E_v$  appears less fragmented and with a lower fraction of lattice defects than the  $77 \text{ J}/\text{mm}^3$  condition. Moreover, regions with fine lamellar  $\alpha+\beta$  microstructure can be observed at higher  $E_v$ , indicating a partial decomposition of  $\alpha'$ . This is in line with results from HEXRD that will be discussed below, which show a significantly smaller FWHM of  $\alpha/\alpha'$ -{100} associated with microstructure (grain/diffracting domain size) and defect density, i.e. a further evidence of partial decomposition of the  $\alpha'$  martensite due to the intrinsically higher heat input at elevated  $E_v$ .

APT shows discontinuous one-dimensional V-enriched features in the low  $E_v = 77 \text{ J}/\text{mm}^3$  condition (Fig. 2(b) and (c)) which may correspond to precursors of stable  $\beta$  since V is the main  $\beta$ -stabilizer in the Ti-6Al-4V alloy. The APT results obtained for the as-built microstructure at  $E_v = 145 \text{ J}/\text{mm}^3$ , in contrast, show V-enriched regions with two-dimensional film-like morphology of similar orientations and a typical thickness of  $\sim 10 \text{ nm}$  (Fig. 2(e) and (f); examples are marked with arrows). The same V-enriched regions

can be seen as bright features in the corresponding SEM micrograph (Fig. 2 (d)), which is likely due to higher content in heavy  $\beta$ -stabilizers and the associated Z-contrast. These regions can thus be identified as  $\beta$ -films in conjunction with HEXRD as discussed below.

In the  $E_v = 145 \text{ J}/\text{mm}^3$  as-built condition, APT reveals even finer details in addition to the already mentioned  $\beta$ -films, namely, parallel, two-dimensional features with a thickness below  $\sim 3 \text{ nm}$ . Examples are marked by black arrows in Fig. 2 (e). These features are less enriched in V than the  $\beta$ -films and hence not enclosed by the iso-concentration surfaces at 8 at.% V.

The presence of  $\beta$ -phase in both studied conditions is evident from HEXRD. A very weak  $\beta$ -{200} peak can be recognized for  $77 \text{ J}/\text{mm}^3$  in Fig. 3 (c) that is more pronounced for the  $145 \text{ J}/\text{mm}^3$  condition (Fig. 3 (b)). In the latter case, it is additionally accompanied by a  $\beta$ -{110} peak. The lower  $E_v$  condition contains a much smaller mass fraction of  $\beta$  as judged from the peak intensities. The  $\beta$ -{200} peak appears at a slightly lower  $2\theta$  angle for the  $77 \text{ J}/\text{mm}^3$  as compared to  $145 \text{ J}/\text{mm}^3$  condition ( $4.3583^\circ$  vs.  $4.3993^\circ$ ), which points to smaller lattice constants of  $\beta$  due to an increase in  $\beta$ -stabilizers in its composition [37]. Since the  $\alpha$  and the  $\alpha'$  phases crystallize in a hexagonal close-packed structure (hcp, space group  $P6_3/\text{mmc}$ ) with similar lattice parameters [38], these cannot be easily distinguished in the HEXRD results and are thus referred to as  $\alpha/\alpha'$ .

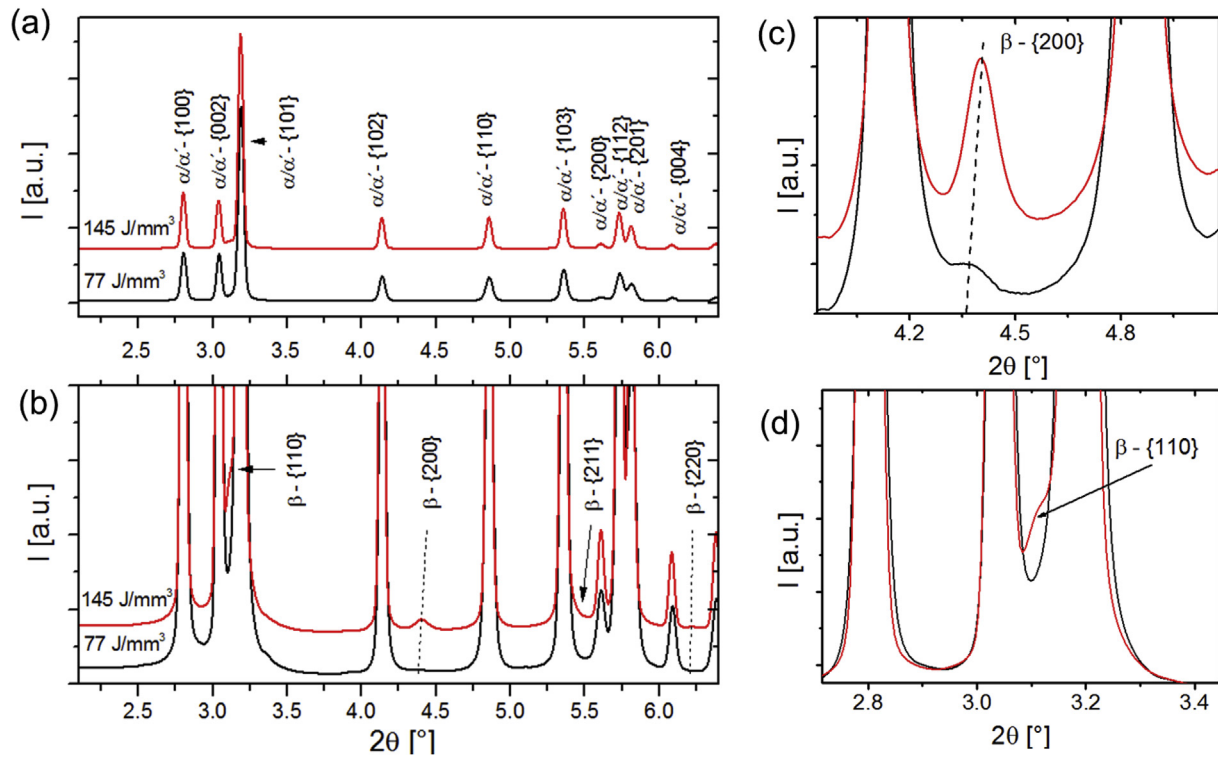


**Fig. 3.** HEXRD diffractograms of the SLM samples in the as-built state ( $E_V = 77 \text{ J/mm}^3$  in black,  $145 \text{ J/mm}^3$  in red): (a) full intensity range of recorded patterns, (b) magnification thereof, (c)  $\beta$ -{200} and (d)  $\beta$ -{110} peaks. (For interpretation of the references to colour in this figure legend, the reader is referred to the Web version of this article.)

### 3.3. Martensite decomposition induced by heat treatments

The phase transformations and microstructural changes of the SLM as-built conditions induced by subsequent heat treatments (section 2.2) were studied as a function of thermal treatment to analyse martensite decomposition leading to precipitation of  $\beta$ . For conciseness reasons, only the HEXRD, SEM and APT results corresponding to  $E_V = 145 \text{ J/mm}^3$  are presented. The results for  $E_V = 77 \text{ J/mm}^3$  at annealing temperatures  $T \geq 530 \text{ }^\circ\text{C}$  are provided as supplementary material (Figs. S1 and S2).

The HEXRD results shown in Fig. 4 indicate that annealing of the  $E_V = 145 \text{ J/mm}^3$  as-built condition at  $400 \text{ }^\circ\text{C}$  for 2 h leads to a slight reduction of peak intensity and a shift of the  $\beta$ -{200} reflection towards higher  $2\theta$  (Fig. 4(d)), which corresponds to a reduction of the  $\beta$ -lattice parameter  $a_\beta$ . This reduction can be associated with an increase of the V-concentration [37] in the  $\beta$ -phase. Noteworthy after annealing at  $400 \text{ }^\circ\text{C}$  is the appearance of diffraction peaks of the  $\alpha_2$  phase ( $\text{Ti}_3\text{Al}$ ; see Fig. 4(c) and Fig. S1), which is only present for this heat treatment in both the low and high  $E_V$  synthesized materials.

No remarkable changes in the microstructure after annealing at  $400 \text{ }^\circ\text{C}$  are observed from SEM (Fig. 5(a)) and APT (Fig. 5(b)) with respect to the as-built condition at  $145 \text{ J/mm}^3$  (Fig. 2(d)–(f)). The  $\beta$ -stabilizer-enriched films are still recognizable. Also the micrographs of the  $77 \text{ J/mm}^3$  condition after annealing at  $400 \text{ }^\circ\text{C}$  (2 h) show qualitatively the same features and phases as its as-built condition (see Supplementary Material Fig. S2).

Annealing of  $E_V = 145 \text{ J/mm}^3$  specimens at  $530 \text{ }^\circ\text{C}$  (2 h) induces a further shift of  $\beta$ -{200} towards higher  $2\theta$  (Fig. 4(c) and (d)). Also  $\beta$ -{211} becomes clearly distinguishable as a shoulder to  $\alpha/\alpha'$ -{103}. Concurrently, the morphology of  $\beta$  becomes fragmented with respect to the as-built state and  $\beta$ -platelets (i.e. large elongated particles) as well as nanometric  $\beta$ -particles are detected by SEM

(Fig. 5(c); some  $\beta$ -particles are indicated by white circles) as well as by APT (Fig. 5(d)). The  $\beta$ -particles are generally below  $\sim 50 \text{ nm}$  in size.

Annealing the high  $E_V$  condition at  $650 \text{ }^\circ\text{C}$  (2 h) yielded only an incremental change compared to the microstructure obtained after the  $530 \text{ }^\circ\text{C}$  heat treatment. The size of the  $\beta$ -particles and their number apparently increased further, their shape now appearing larger and more elongated towards extended two-dimensional precipitates (e.g. platelets or even film-like; Fig. 6(a) and (b)). On the other hand, the  $\beta$ -{200} reflection shifts to lower  $2\theta$  (Fig. 4(b)), compatible with a V concentration decrease, while intensity increases of the  $\beta$ -{200} and  $\beta$ -{211} peaks point to a growth of the  $\beta$  mass fraction.

Annealing at  $800 \text{ }^\circ\text{C}$  (2 h) leads to a lamellar  $\alpha + \beta$  microstructure with semi continuous  $\beta$ -films between lamellae (Fig. 6(c)–(d)), although this time they are wider and more continuous than at lower annealing temperatures. The microstructure appears significantly coarsened and stabilized, i.e. showing fewer defects compared to the martensitic as-built state as result of significant martensite decomposition [11,13,29,39]. The  $\beta$ -films are typically around  $100$ – $200 \text{ nm}$  in width, while the  $\alpha$ -laths show a wider size distribution with widths between  $\sim 0.5$  and  $2 \mu\text{m}$  and lengths varying from below  $0.5 \mu\text{m}$  to above  $20 \mu\text{m}$ . This transformation is accompanied by a further shift of the  $\beta$ -peaks towards lower  $2\theta$  together with an increase of their intensity (Fig. 4(b)–(d)).

The HEXRD results provide additional insights on the martensite decomposition and the changing composition of the  $\beta$ -phase that complement the APT and SEM observations. The analysis of the  $\beta$ -diffraction signals shows that  $a_\beta$  for the  $145 \text{ J/mm}^3$  condition drops from  $0.323$  to  $0.319 \text{ nm}$  (Fig. 7(a)) between the as-built and  $530 \text{ }^\circ\text{C}$  (2 h) states, pointing to increasing V-concentration in the  $\beta$ -phase. Conversely, the heat treatments at  $650 \text{ }^\circ\text{C}$  and  $800 \text{ }^\circ\text{C}$  in turn raise  $a_\beta$  to  $0.321 \text{ nm}$ , suggesting a loss of V [37]. Coinciding with the

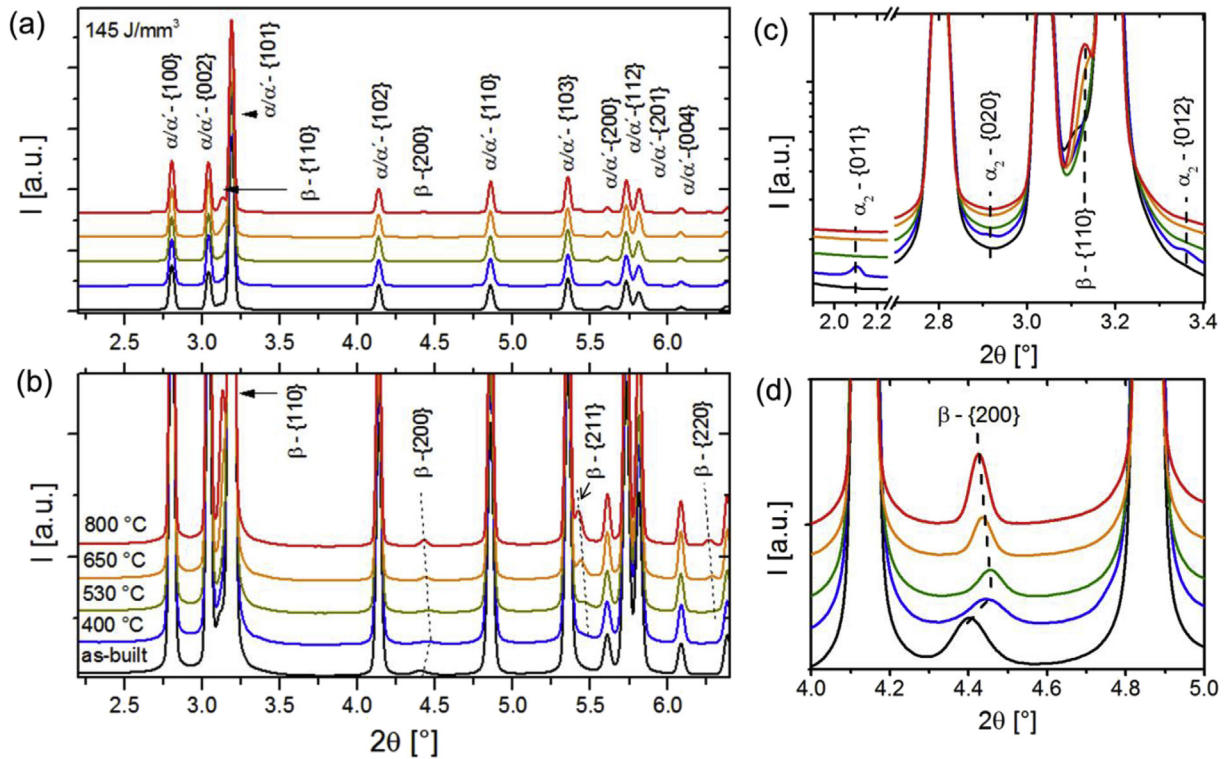


**Fig. 4.** (a) HEXRD of  $E_V = 145 \text{ J/mm}^3$  as-built condition and heat treated at the indicated temperatures for 2 h and (b) intensity magnification thereof. (c) Regions with  $\alpha_2$  diffraction peaks and  $\beta$ -{110}. (d) Evolution of  $\beta$ -{200}.

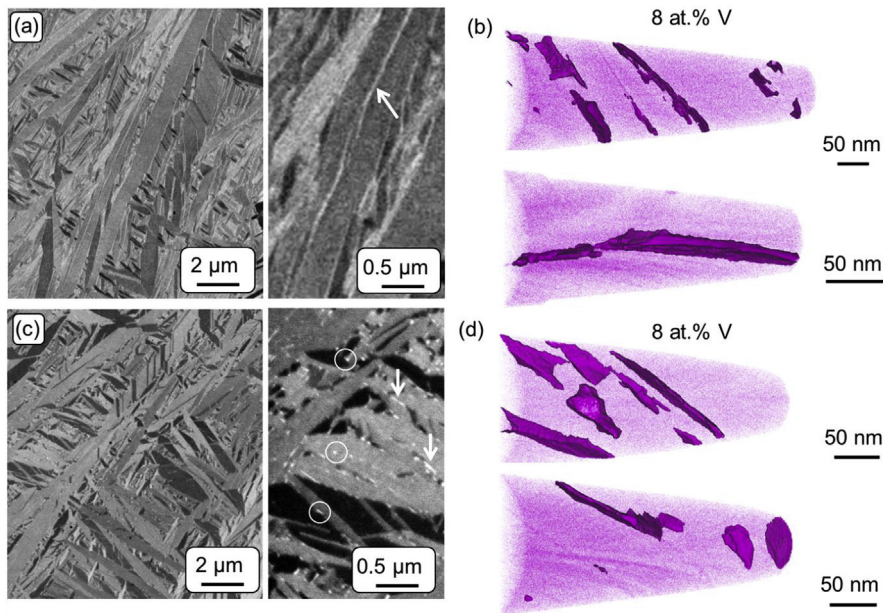


**Fig. 5.** Microstructure evolution upon post heat treatment of the  $E_V = 145 \text{ J/mm}^3$  condition: (a) SEM-BSE micrographs and (b) V distribution obtained by APT from samples annealed at 400 °C (2 h). (c) SEM-BSE micrographs and (d) V distribution obtained by APT from samples annealed at 530 °C (2 h). A threshold of 8 at.% V was chosen for all displayed iso-concentration surfaces. Circles indicate  $\beta$ -particles, arrows two-dimensional platelet or film-like  $\beta$ .

minimum of  $a_\beta$  at 530 °C, the  $\beta$ -mass fraction  $f_\beta$  begins to increase upon annealing at this temperature following a fairly linear trend up to 650 °C and then slowing down up to 800 °C (Fig. 7 (b)). The  $\beta$ -precipitates observed after heat treatments of the as-built materials in the temperature range of 650–800 °C result in ca. 4–5 wt.% of  $\beta$ -phase.

The increase in  $f_\beta$  picking up at  $T > 400$  °C is mirrored by a systematic reduction of the FWHM of  $\alpha/\alpha'$ -{100} (Fig. 7 (c)), which can be attributed to the decomposition of  $\alpha'$  towards a more stable microstructure closer to  $\alpha$  in association with coarsening of the  $\alpha/\alpha'$  grains [15]. The FWHM of the as-built condition at low  $E_V$  is significantly larger than that of the  $E_V = 145 \text{ J/mm}^3$  state,

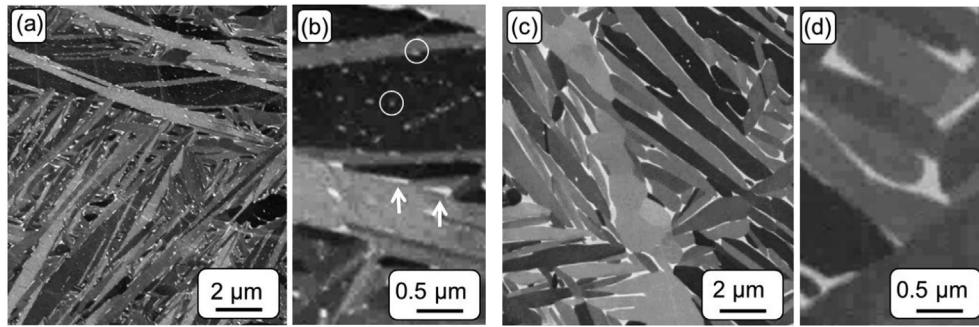


Fig. 6. SEM-BSE results of  $E_V = 145 \text{ J/mm}^3$  condition heat treated at: (a), (b) 650 °C (c), (d) 800 °C for 2 h each. Circles in (b) indicate  $\beta$ -particles and arrows film-like  $\beta$ .

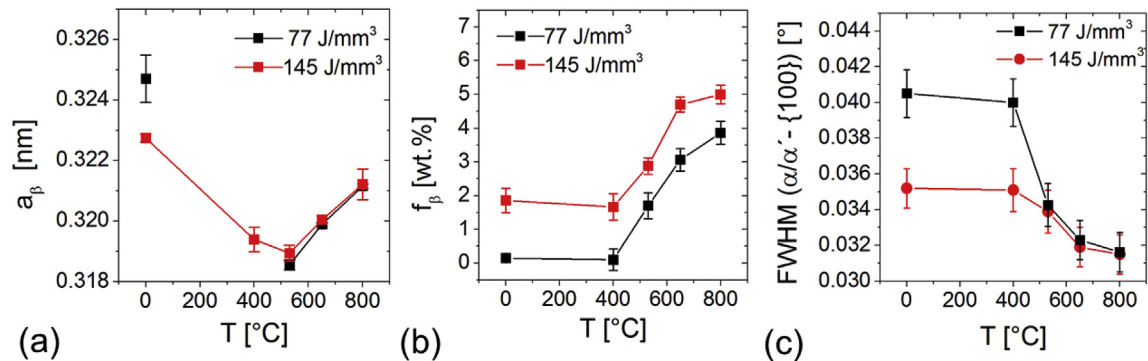


Fig. 7. Evolution of (a)  $\beta$ -lattice parameters,  $a_\beta$ , (b) the  $\beta$ -mass fraction  $f_\beta$  and (c) FWHM of  $\alpha/\alpha'$ -{100} for  $E_V = 77$  and  $145 \text{ J/mm}^3$ .

suggesting the intrinsic heat input led to a higher degree of  $\alpha'$  to  $\alpha$  phase transformation in line with the more stabilized microstructure observed in SEM (Fig. 2). Also, relief of strain fields associated with lattice distortions [40], which can be expected upon transformation of strained colonies of fine  $\alpha'$  laths to thermodynamically more stable  $\alpha$  lamellae, can play a role for the narrowing of the peak width. Hence, in this case the FWHM of  $\alpha/\alpha'$  can be used as indicator for the transformation of the martensitic as-built state into the  $\alpha/\beta$ -microstructure.

The low  $E_V = 77 \text{ J/mm}^3$  as-built condition is characterized by an  $a_\beta$  lattice parameter of 0.325 nm, which is larger than that for the  $E_V = 145 \text{ J/mm}^3$  condition. This value is close to the one obtained for nearly fully martensitic SLM samples analysed by Xu et al. [20] (0.326 nm). It suggests that the  $\beta$  phase present in this condition has a low V content and may either be retained from solidification and cooling from the  $\beta$ -field, or be due to a lesser degree of intrinsic heat input than achieved with the current  $E_V = 145 \text{ J/mm}^3$  parameters. Simultaneously, the FWHM of the  $\alpha/\alpha'$ -{100} peak exceeds that of  $E_V = 145 \text{ J/mm}^3$  significantly, which may be a consequence of the higher density of lattice defects. After annealing at 400 °C the  $\beta$ -phase is no longer detected by HEXRD, whereas after heat treatments in the 530 °C–800 °C temperature range, similar  $a_\beta$  and  $\alpha/\alpha'$ -{100} FWHM compared to those of the samples built at  $E_V = 145 \text{ J/mm}^3$  are found (Figs. 5 and 6 and S2).

#### 3.4. Vickers hardness changes of the different microstructure conditions

The phase- and microstructure transformations induced by the different post annealing treatments of the two as-built conditions lead to significantly varying Vickers hardness values (HV; Fig. 8): HV increases from the as-built states (~395 HV on average) to ~405 HV after annealing at 400 °C (2 h) and 530 °C (2 h). The heat

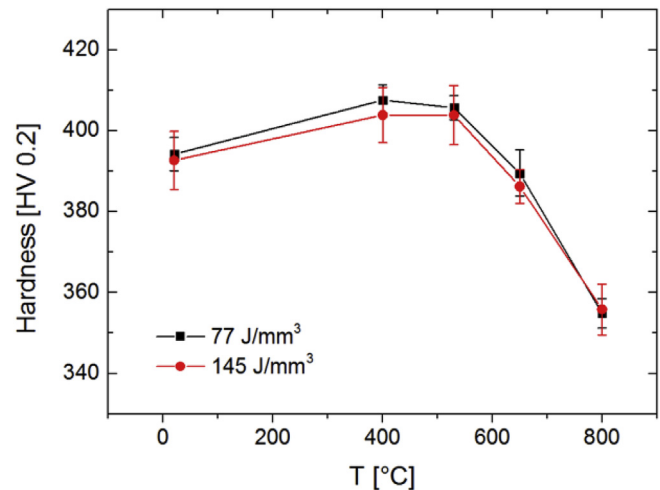


Fig. 8. Vickers hardness  $HV_{0.2}$  of samples built at  $E_V = 77 \text{ J/mm}^3$  (black) and  $145 \text{ J/mm}^3$  (red): as-built and heat treated to 400 °C, 530 °C, 650 °C and 800 °C. Each data point corresponds to an average of 100 measured indents. (For interpretation of the references to colour in this figure legend, the reader is referred to the Web version of this article.)

treatments at higher temperatures of 650 °C (2 h) lead to a sizable drop to ~380 HV and ~350 HV after post annealing to 800 °C (2 h).

## 4. Discussion

### 4.1. Compositional analysis and element partitioning

The  $a_\beta$  lattice constant changes and the formation of new one- and two-dimensional  $\beta$ -precipitates upon annealing of the as-built

SLM materials indicate compositional changes of the  $\beta$ -phase that result from the diffusion-limited martensite decomposition [10,11,13,22]. It is linked with energy (heat) introduced to the SLM as-built material directly by the laser or by post-annealing [3,9–11,20]. Hence, the larger fraction of newly-formed as well as retained  $\beta$  for the  $E_V = 145 \text{ J/mm}^3$  condition results from the intrinsically higher energy density (stronger intrinsic heat treatment) introduced during SLM, whereas at  $E_V = 77 \text{ J/mm}^3$  the intrinsic heat treatment effects are much weaker (Fig. 7 (b)).

Xu et al. [11] found that martensite in a fine acicular as-built state decomposes already significantly upon annealing of SLM-produced Ti-6Al-4V at temperatures as low as  $400^\circ\text{C}$  (2 h), leaving a fine lamellar  $\alpha/\beta$  structure with thin  $\beta$ -films. Analogous to our results, fine  $\beta$ -particles were formed after annealing at  $540^\circ\text{C}$  [10]. However, the results obtained by HEXRD in the present work show that martensite decomposition becomes only significant at annealing temperatures above the range of ca.  $400^\circ\text{C}$ , as reported by Xu et al. and others [10,11,22]. Only after annealing at  $530^\circ\text{C}$  clear signs of martensite decomposition can be observed from the increase of the  $\beta$ -volume fraction and decrease of the FWHM of  $\alpha/\alpha'$  (Fig. 7). In line with our HEXRD results, Wu et al. obtained a  $\beta$ -phase in film morphology by annealing SLM processed Ti-6Al-4V at  $500^\circ\text{C}$  [13], which led to a maximum in hardness.

Martensite decomposition is accompanied by diffusive partitioning of  $\alpha$ - and  $\beta$ -stabilizing elements in SLM Ti-6Al-4V. In order to analyse the composition changes of the  $\beta$ -precipitates, the average chemical composition of the regions enriched with  $\beta$ -stabilizers were computed from APT proximity histograms in the as-built state and after annealing at  $400^\circ\text{C}$  and  $530^\circ\text{C}$  for the high  $E_V$  condition, respectively (Table 4). For better legibility, only one exemplary data set of a sample annealed at  $530^\circ\text{C}$  (2 h) is presented in Fig. 9 below. This annealing state already shows well developed  $\beta$ -phase (fragmented two-dimensional platelet-shaped as well as small particulate  $\beta$ ; the dataset of Fig. 9 is the same as in Fig. 5 (d)).

The two initial as-built conditions at low and high  $E_V$  (Supplementary Figs. S3 and S4) exhibit a qualitatively similar behaviour, i.e. element partitioning between matrix and the  $\beta$ -stabilizer-enriched features is observed from the rejection of Al and O and the increase in V and Fe in the latter regions (Fig. S3 (c) and Fig. S4 (c)). The stronger intrinsic heat treatment effect introduced by processing at higher energy density  $E_V = 145 \text{ J/mm}^3$  compared to  $77 \text{ J/mm}^3$  leads to a stronger partitioning, particularly for V and Fe (Table 4).

The subsequent annealing of the  $E_V = 145 \text{ J/mm}^3$  condition at intermediate temperatures of  $400^\circ\text{C}$  (Fig. S5) and  $530^\circ\text{C}$  (Fig. 9) enhanced this trend. The composition of the  $\beta$ -stabilizer-enriched regions decreased further in  $\alpha$ -stabilizers while the V- and Fe-concentrations increased to as much as  $\sim 18$ – $20 \text{ at.}\%$  and  $\sim 8 \text{ at.}\%$ ,

respectively (Table 4). The diffusion kinetics appear to be sufficiently fast at  $530^\circ\text{C}$  in order to reach a  $\beta$ -phase with V content close to that expected from the Ti-6Al-4V equilibrium phase diagram [41,42].

In general, the increasing rejection of Al from the  $\beta$ -precipitates [37,43] and their enrichment with Fe and V from the surrounding matrix after the  $400^\circ\text{C}$  (2 h) and  $530^\circ\text{C}$  heat treatments correlates well with the decrease of  $a_\beta$  observed in HEXRD (Fig. 7 (a)). The trends observed for the V content and  $a_\beta$  agree well with previous reports from Castro et al. [44]. In particular, Castro et al. obtained for Ti-6Al-4V ingots annealed at  $530^\circ\text{C}$  a V content of  $\sim 17 \text{ at.}\%$  in  $\beta$  [44], which is close to the value of  $18 \text{ at.}\%$  obtained here from APT probing. Consistently, annealing at an elevated temperature of  $850^\circ\text{C}$  (2 h) was reported to result in a decrease to  $\sim 16 \text{ at.}\%$  V in  $\beta$ -films [22].

Moreover, the partitioning of V observed for the  $530^\circ\text{C}$  annealed condition is well in line with reports of EBM Ti-6Al-4V samples manufactured at  $600^\circ\text{C}$ – $650^\circ\text{C}$  (up to  $24 \text{ at.}\%$  in  $\beta$  for 10 mm thick samples) [30]. Fine  $\beta$ -laths ( $< \sim 30 \text{ nm}$ ) were reported to contain slightly more V than the wider  $\beta$ -features, suggesting that they formed at lower temperatures [20].

The different degrees of elemental partitioning can be seen more clearly by means of the partitioning ratio  $k^{-1} = C_\beta/C_\alpha$  (Fig. 10), where  $C_\beta$  is the concentration inside the enriched features and  $C_\alpha$  outside these regions.  $C_\alpha$  and  $C_\beta$  can be computed from the APT proximity histograms. High partitioning ratios point to a strong accumulation of an element in these regions, while  $k^{-1} < 1$  indicate depletion.

The partitioning ratios clearly evidence a much stronger tendency of Fe ( $k^{-1}$  from  $\sim 15$  to  $\sim 106$ ) to accumulate in the  $\beta$ -phase with increasing SLM energy density  $E_V$  (as-built, i.e. due to intrinsic heat treatment) and, even more so, with increasing annealing temperature than found for V ( $\sim 2.5$ – $\sim 7.3$ ). The latter values are only slightly below those obtained for V in  $\beta$  for Ti-6Al-4V produced by EBM [30] ( $k^{-1}$  from  $\sim 8.9$ – $10.7$ ) despite much higher build platform temperatures used in EBM. While partitioning of Fe ( $k^{-1} = \sim 20.5$ – $20.9$ ) and O ( $k = \sim 1.7$ – $2.1$ ) appeared to be less pronounced for EBM, the partitioning of Al into  $\alpha$  ( $k = \sim 3.4$ – $4.1$ ) was found to be stronger [30].

#### 4.2. Implications of the microstructure changes for hardness

The measured changes in Vickers hardness are in line with previous studies of post-annealing SLM Ti-6Al-4V [8,13,22], showing an increase of HV from as-built to intermediate subtransus annealed conditions (with a maximum around  $500^\circ\text{C}$  [13] to  $600^\circ\text{C}$  [22]) and a sizable decline for heat treatments above  $550$ – $600^\circ\text{C}$ .

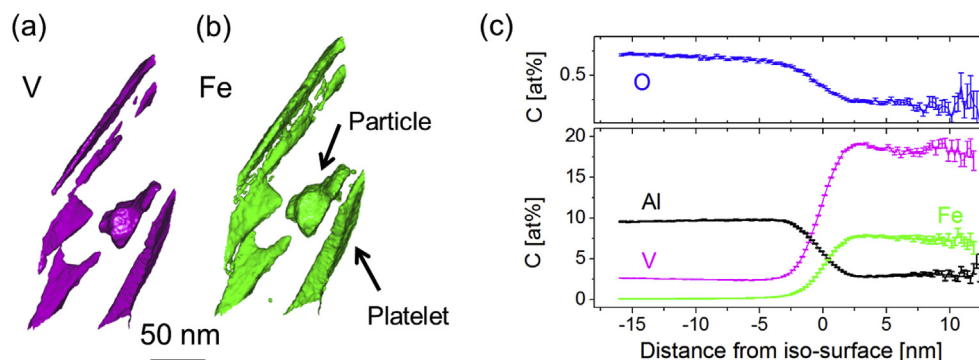
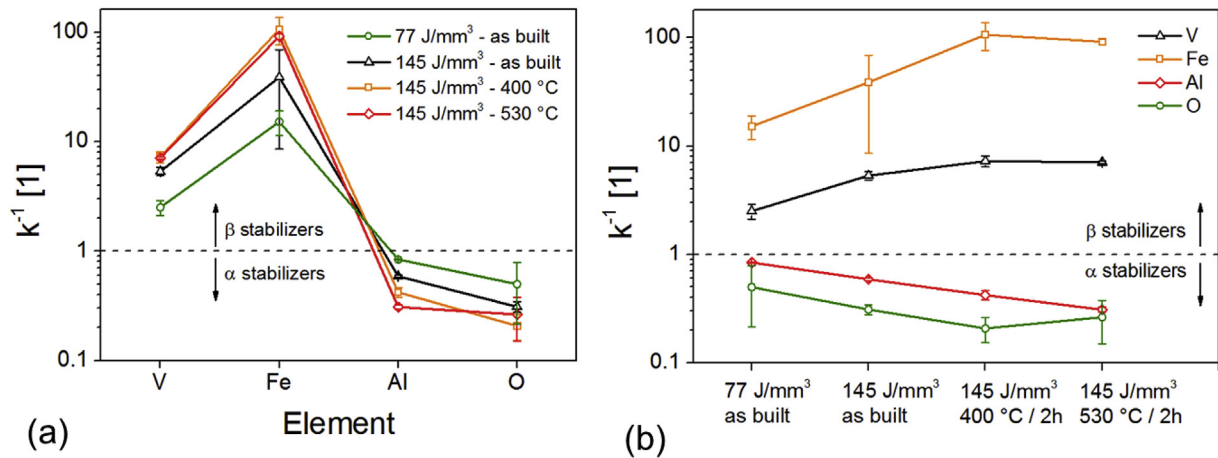


Fig. 9. APT results of the  $E_V = 145 \text{ J/mm}^3$  condition heat treated at  $530^\circ\text{C}$  for 2 h. (a) reconstructed volume showing a V-iso-concentration surface at 8 at.%, (b) Fe-iso-concentration surface 1 at.%, (c) a proximity histogram with distance measured from the corresponding 4 at.% Fe-iso-surface.

**Table 4**  
Average element concentrations [at.%] determined from APT proximity histograms (HT = heat treated). For comparison: the Ti-6Al-4V feedstock consists of 10.8 at.% Al, 3.6 at.% V, 0.16 at.% Fe and 0.31 at.% O.

Phase	Elements	77 J/mm <sup>3</sup> , 'as-built' (Fig. S3)	145 J/mm <sup>3</sup> , 'as-built' (Fig. S4)	145 J/mm <sup>3</sup> , HT 400 °C (Fig. S5)	145 J/mm <sup>3</sup> , HT 530 °C (Fig. 9 and Fig. S6)
Regions enriched with $\beta$ -stabilizers	V	10.0	16.0	20.0	18.0
	Fe	2.5	3.3	5.0	7.7
	Al	8.5	5.5	4.5	3.0
	O	0.4	0.3	0.1	0.2
$\alpha/\alpha'$	V	3.6	3.0	2.8	2.6
	Fe	0.2	0.2	0.1	0.1
	Al	10.2	9.5	9.8	9.6
	O	0.5	0.9	0.4	0.7
average concentration in the sample	V	3.6	3.5	3.8	3.5
	Fe	0.1	0.2	0.2	0.4
	Al	10.3	9.5	9.4	9.4
	O	0.3	0.4	0.4	0.7



**Fig. 10.** Element partitioning ratio  $k^{-1} = C_{\beta}/C_{\alpha}$  derived from the APT data. (a) Partitioning ratios for the  $\beta$ - and  $\alpha$ -stabilizers V and Fe as well as Al and O, respectively. (b) Partitioning ratios for the different SLM and heat treated conditions.

The initial increase of the hardness (Fig. 8) from ~395 HV ('as-built') to ~405 HV (400 °C) can be linked to the formation of the new  $\alpha_2$ -phase as deduced from HEXRD since concurrently no major change in the  $\alpha/\alpha'$  matrix or the  $\beta$ -films was detected.

The subsequent hardness plateau of ~405 HV (Fig. 8) observed for annealing between 400 and 530 °C can be explained by the changes of the  $\beta$ -phase as detected by HEXRD. Starting with the 400 °C annealing and becoming pronounced for 530 °C, the formation of the fine, nanometric  $\beta$ -particles in the  $\alpha/\alpha'$  grains might act to retain a high hardness despite the disappearance of  $\alpha_2$ . Small residual amounts of  $\alpha_2$ -Ti<sub>3</sub>Al below the HEXRD detection limit might still be present and enhance dislocation pinning.

The hardness decrease after heat treatments at  $T \geq 650$  °C can be linked to coarsening of the lamellar  $\alpha/\alpha'+\beta$  microstructure, which is in line with the Hall-Petch relationship [45]. Furthermore, the transformation of the  $\beta$ -phase into coarse  $\beta$ -films and the simultaneous increase in its overall fraction can lead to a decreasing hardness since the  $\beta$ -Ti phase shows a lower hardness compared to  $\alpha$ -Ti [46]. This, combined with the progressing martensite decomposition during the transformation into more stabilized, less defective  $\alpha/\beta$  microstructures, lowers HV further when annealing up to 800 °C.

#### 4.3. Nucleation of $\beta$ -phase at lattice defects

Closer analysis of the APT results provides further insights into the nucleation sites of the  $\beta$ -phase. Concentration profiles determined across regions of specific features in the APT volumes allow

detailed analysis of their size, morphology and local chemistry.

While the distribution of Fe in the 145 J/mm<sup>3</sup> as-built condition (Fig. 11), another strong  $\beta$ -stabilizer, mimics the  $\beta$ -films from the SEM micrographs (Fig. 2 (d)), it also reveals finer details on less enriched structures that were only vaguely recognizable in the V distribution (Fig. 2 (e)). These details consist of one- and two-dimensional regions enriched with these  $\beta$ -stabilizers: nanometric "columnar" features (Fig. 11, labels 1 and 2) extending perpendicularly from the thin film-like regions (labels 3 and 4). A video with a 3D representation of the APT data is provided in the supplementary material (Supplementary video related to this article can be found at <https://doi.org/10.1016/j.actamat.2019.01.039>). Similar features have previously been attributed to enrichments at lattice defects in other metallic systems produced by conventional metallurgical synthesis methods [47–49].

Supplementary video related to this article can be found at <https://doi.org/10.1016/j.actamat.2019.01.039>.

The columnar features show an elongated, ellipsoidal base ~1.5 nm in width (FWHM from concentration profiles C1 and C2, Fig. 11(g) and (h), respectively) and measure ~10 nm in length. They can be attributed to enrichment at one-dimensional lattice defects such as dislocations and dissociated (partial) dislocations [47,48]. These features possibly represent formation sites, i.e. precursors of  $\beta$ , which would be in line with previous studies suggesting  $\beta$ -nucleation not only at interfaces within individual  $\alpha'$  martensite plate boundaries, but also at similar lattice defects within  $\alpha'$  needles [3,30].

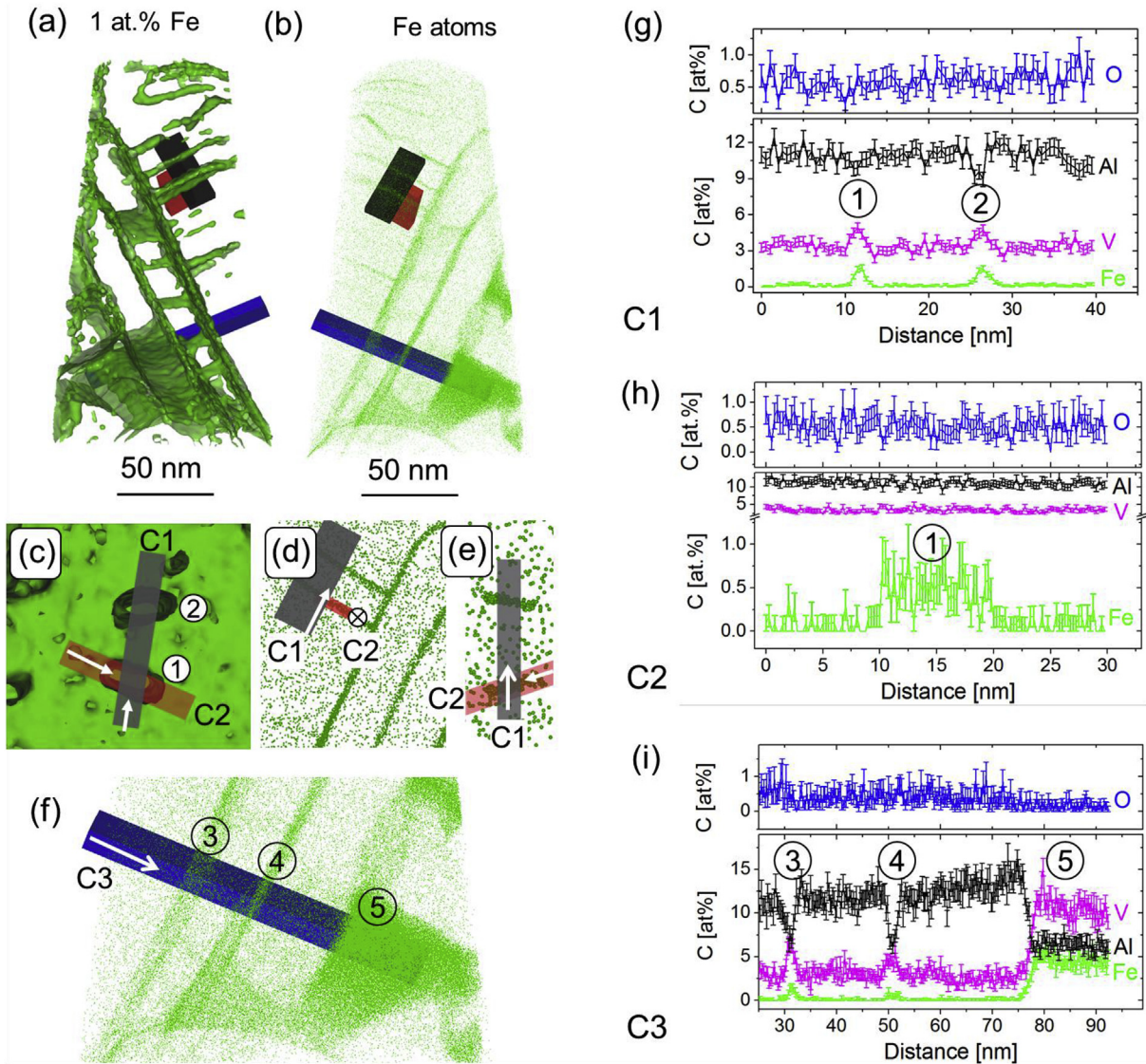


**Fig. 11.** APT analysis (voltage mode) of the  $E_V = 145 \text{ J/mm}^3$  as-built material (same APT reconstruction as shown for V in Fig. 2 (e)): (a) iso-concentration surface at 1 at.% Fe, (b) depicts all Fe atoms in the reconstruction as green dots. (c)–(e) magnified insets of features assigned to Fe-enrichment at one-dimensional lattice defects such as dislocations (label 1 and 2); the black and red rectangles mark the boxes along which the 1D concentration profiles in (g) and (h) were computed. In (c) an iso-concentration surface at 1 at.% Fe is shown in green. In (d) all Fe atoms in a 5 nm thick slice through the reconstruction are shown as green circles, (e) depicts all Fe atoms in a 10 nm slice rotated  $90^\circ$  compared to (d). (f) cross section (slice of 20 nm through the reconstruction) through two-dimensional enrichments (labels 3, 4) and a developed  $\beta$ -phase (label 5). The insets show the positions of the rectangles (C1–C3) used for determining concentration profiles (g)–(i); the arrows indicate the direction of the rectangles' longitudinal axis. (For interpretation of the references to colour in this figure legend, the reader is referred to the Web version of this article.)

Interestingly, the concentration profiles measured across these columnar features (Fig. 11(g) and (h); Table 4) show that they are much less enriched in V (~5 at.%) and Fe (~1.5 at.%) as compared to the fully developed  $\beta$ -phase (Fig. 11 (f); label 5). The latter  $\beta$ -phase precipitate contained ~11 at.% V and ~4 at.% Fe. No significant amounts of O were detected in the columnar features and Al evidenced a rather high fraction of up to ~10 at.%.

The width of the two-dimensional film-like regions enriched in V and Fe (Fig. 11 (f), labels 3 and 4) vary from less than ~2 nm to up to 3 nm (Fig. 11 (i)). Thus, they appear much narrower than the developed  $\beta$ -films (~10 nm). The concentration profiles analysed across these two structures again signify a less pronounced enrichment in  $\beta$ -stabilizers compared to the  $\beta$ -phase: ~5.5 at.% V and ~1 at.% Fe. Taking into consideration the narrow width as well as the composition closer to a super-saturated martensite, these features are markedly different from the fully developed  $\beta$ -films

and may be assigned to a precursor state of the  $\beta$ -phase located at  $\alpha'$  martensite plate boundaries.

Analogously, the local compositions in the nanometric  $\beta$ -precursors in the low  $E_V = 77 \text{ J/mm}^3$  as-built condition (Fig. S3) also differs significantly in terms of V (~6 at.%) and Fe (~1.6 at.%) from the more developed  $\beta$ -phase (Table 4).

The changes of the  $\beta$ -phase after annealing are likewise mirrored in the Fe distributions: After annealing the  $145 \text{ J/mm}^3$  condition at  $400^\circ \text{C}$  (Fig. S5) again  $\beta$ -films measuring ~10 nm in width (derived from the concentration profiles in Fig. S5 (g)) are detected that are, hence, morphologically similar to the  $\beta$ -films in the as-built state. The local amounts of V and Fe in these  $\beta$ -films are, however, now increased to ~27 at.% and ~7 at.% from the as-built state, again providing evidence of the partitioning from the martensite decomposition (Table 5). Similarly, the fragmented two-dimensional  $\beta$ -platelets and the nanometric  $\beta$ -particles of the

**Table 5**  
Comparison of local concentrations [at. %] of elements in particular microstructure features determined from APT concentration profiles.

Sample	Features	V	Fe	Al	O	Fig.
77 J/mm <sup>3</sup> As-built	Precursors of $\beta$ -phase	6.3	1.6	7.8	0.2	Fig. S3
145 J/mm <sup>3</sup> As-built	<b>1D lattice defects</b> (e.g. dislocations/partial dislocations)	4.9/4.7	1.6/1.5	9.8/9.0	0.5	Fig. 11: C1/C2
	<b>2D lattice defects</b> (e.g. twins, low angle GB)	6.2/4.5	1.5/0.5	6.8/5.0	0.5	Fig. 11: C3
	<b><math>\beta</math>-films</b>	11	4.0	6.5	0.2	Fig. 11: C3 Fig. S4
145 J/mm <sup>3</sup> 400 °C	<b><math>\beta</math>-films</b>	27	6.6	3.1	0.2	Fig. S5
145 J/mm <sup>3</sup> 530 °C	<b><math>\beta</math>-particles</b>	32	6.1	2.0	0.1	Fig. 12 (a)
	<b><math>\beta</math>-platelets/films</b>	22	5.5	2.7	0.1	Fig. 12 (c)

145 J/mm<sup>3</sup>/530 °C condition are also found in the Fe reconstruction from APT (Fig. 12). The small  $\beta$ -particles measure roughly  $\sim 50 \text{ nm} \times \sim 6 \text{ nm}$  in size. Particularly the increase in V is quite pronounced in these features, but a sizable spread can be inferred: the  $\beta$ -platelet showed  $\sim 22 \text{ at.}\% \text{ V}$  (Fig. 12 (d)), whereas the  $\beta$ -nanoparticle contained up to 32 at.% V (Fig. 12 (b)).

From these results it can be concluded that the element partitioning that leads to growth of the  $\beta$ -phase can be tracked back with APT from the less enriched regions at lattice defects in the as-built state to the films/platelets and nano-particles. These observations support that the early enrichment stages occurring at lattice defects play a key role in  $\beta$ -phase nucleation within  $\alpha'$ -matrices in SLM Ti-6Al-4V. Particularly the two-dimensional enrichments located at lattice defects may be considered as precursors for  $\beta$ -film formation.

## 5. Conclusions

The formation and evolution of the microstructure in SLM Ti-6Al-4V was studied in as-built condition and upon sub-transus annealing between 400 and 800 °C focusing on element partitioning and the role of lattice defects on precipitation of the  $\beta$  phase. The as-built materials were produced with two sets of SLM

parameters at the extremes of the process window optimized for low porosity and short processing times. The following conclusions are drawn:

- The as-built condition manufactured at low  $E_V = 77 \text{ J/mm}^3$  (weak intrinsic heat input) shows almost exclusively fine acicular  $\alpha'$  martensitic microstructures with small amounts of  $\beta$  (presumably retained) and  $\beta$ -precursors. The stronger intrinsic heat treatment effects at higher  $E_V = 145 \text{ J/mm}^3$  processing parameters leads to continuous two-dimensional features attributed to  $\beta$ -films. Both types of microstructures are far from thermodynamic equilibrium.
- Upon annealing to 530 °C, the  $\beta$ -films began to fragment into two-dimensional platelets and one-dimensional nanosized  $\beta$ -precipitates, whereas annealing to 800 °C led to a more stabilized, coarse-lamellar  $\alpha/\beta$ -microstructure.
- The changes in the microstructures were mirrored by increased Vickers hardness after annealing to 400 °C (2 h) and 530 °C (2 h), which correlate with the presence of either  $\alpha_2$  (400 °C) and fine  $\beta$ -particles (530 °C) likely pinning dislocation movement. At higher annealing temperatures the hardness dropped due to coarsening of the microstructure and increasing  $\beta$  fractions.

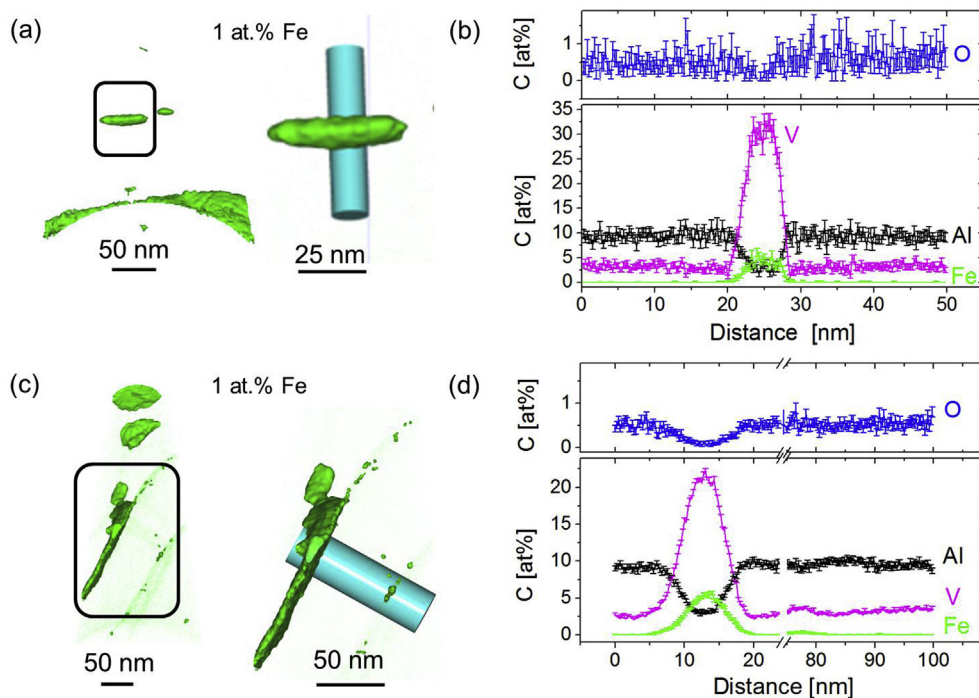


**Fig. 12.** APT results of the Fe-distribution for the condition  $E_V = 145 \text{ J/mm}^3$  heat treated at 530 °C for 2 h: (a)  $\beta$ -particle (iso-concentration surface at 1 at.% Fe) and region of the cylinder for concentration profile analysis; (c) two-dimensional  $\beta$ -precipitate (iso-concentration surface at 1 at.% Fe) and position of the corresponding cylinder; (b) and (d) provide the concentration profiles along the cylinders.

- Martensite decomposition upon annealing leads to substantial element partitioning: Al and O is accumulated in the  $\alpha/\alpha'$  phase, while V and Fe are rejected and diffuse into the  $\beta$ -phase. The partitioning ratio of Fe is one order of magnitude higher than that of V.
- The as-built microstructure produced with  $E_V = 145 \text{ J/mm}^3$  SLM parameters showed additional features assigned to  $\beta$ -precursors at one- and two-dimensional lattice defects. They were slightly more enriched in Fe than in V but contained substantially less  $\beta$ -stabilizing elements than developed  $\beta$ -precipitates. Particularly the two-dimensional features may be precursors for precipitation of  $\beta$  within  $\alpha'$  laths, indicating that lattice defects can indeed be exploited as precipitation site for  $\beta$  in SLM Ti-6Al-4V materials.

## Declarations of interest

None.

## Funding

This work was supported by the German Aerospace Center. The funding source had no involvement of any kind in this study.

## Acknowledgements

DESY is acknowledged for the provision of synchrotron radiation facilities in the framework of the proposals I-20150533 EC and I-20180384 EC, respectively. T. Merzouk is acknowledged for the preparation of SLM samples and P. Watermeyer for the support during SEM investigations. The authors are grateful to U. Tezins and A. Sturm for their support to the FIB and APT facilities at MPIE.

## Appendix A. Supplementary data

Supplementary data to this article can be found online at <https://doi.org/10.1016/j.actamat.2019.01.039>.

## References

- [1] C. Körner, Additive manufacturing of metallic components by selective electron beam melting — a review, *Int. Mat. Rev.* 61 (2016) 361–377.
- [2] S.L. Sing, J. An, W.Y. Yeong, F.E. Wiria, Laser and electron-beam powder-bed additive manufacturing of metallic implants: a review on processes, materials and designs, *J. Orthopaed. Res.* 34 (2016) 369–385.
- [3] P. Barriobero-Vila, J. Gussone, J. Haubrich, S. Sandlöbes, J. Da Silva, P. Cloetens, N. Schell, G. Requena, Inducing stable  $\alpha + \beta$  microstructures during selective laser melting of Ti-6Al-4V using intensified intrinsic heat treatments, *Materials* 10 (2017) 268.
- [4] C. Leyens, M. Peters, Titanium and Titanium Alloys: Fundamentals and Applications, Wiley-VCH (John-Wiley Sons), Weinheim (Chichester), 2003.
- [5] B. Dutta, F.H. Froes, Additive manufacturing of titanium alloys, *Adv. Mater. Process.* 172 (2014) 18–23.
- [6] L.E. Murr, E.V. Esquivel, S.A. Quinones, S.M. Gaytan, M.I. Lopez, E.Y. Martinez, F. Medina, D.H. Hernandez, E. Martinez, J.L. Martinez, S.W. Stafford, D.K. Brown, T. Hoppe, W. Meyers, U. Lindhe, R.B. Wicker, Microstructures and mechanical properties of electron beam-rapid manufactured Ti-6Al-4V biomedical prototypes compared to wrought Ti-6Al-4V, *Mat. Char.* 60 (2009) 96–105.
- [7] L. Thijs, F. Verhaeghe, T. Craeghs, J. Van Humbeeck, J.P. Kruth, A study of the micro structural evolution during selective laser melting of Ti-6Al-4V, *Acta Mater.* 58 (2010) 3303–3312.
- [8] T. Vilaro, C. Colin, J.D. Bartout, As-Fabricated and heat-treated microstructures of the Ti-6Al-4V alloy processed by selective laser melting, *Met. Mat. Trans. A Phys. Metallurgy* 42A (2011) 3190–3199.
- [9] M. Simonelli, Y.Y. Tse, C. Tuck, The formation of  $\alpha + \beta$  microstructure in as-fabricated selective laser melting of Ti-6Al-4V, *J. Mat. Res.* 29 (2014) 2028–2035.
- [10] W. Xu, M. Brandt, S. Sun, J. Elambasseril, Q. Liu, K. Latham, K. Xia, M. Qian, Additive manufacturing of strong and ductile Ti-6Al-4V by selective laser melting via in situ martensite decomposition, *Acta Mater.* 85 (2015) 74–84.
- [11] W. Xu, S. Sun, J. Elambasseril, Q. Liu, M. Brandt, M. Qian, Ti-6Al-4V additively manufactured by selective laser melting with superior mechanical properties, *JOM* 67 (2015) 668–673.
- [12] J.J. Yang, H.C. Yu, J. Yin, M. Gao, Z.M. Wang, X.Y. Zeng, Formation and control of martensite in Ti-6Al-4V alloy produced by selective laser melting, *Mat. Des.* 108 (2016) 308–318.
- [13] S.Q. Wu, Y.J. Lu, Y.L. Gan, T.T. Huang, C.Q. Zhao, J.J. Lin, S. Guo, J.X. Lin, Microstructural evolution and microhardness of a selective-laser-melted Ti-6Al-4V alloy after post heat treatments, *J. Alloy. Comp.* 672 (2016) 643–652.
- [14] G. Kasperovich, J. Haubrich, J. Gussone, G. Requena, Correlation between porosity and processing parameters in TiAl6V4 produced by selective laser melting, *Mat. Des.* 105 (2016) 160–170.
- [15] S. Cao, R.K. Chu, X.G. Zhou, K. Yang, Q.B. Jia, C.V.S. Lim, A.J. Huang, X.H. Wu, Role of martensite decomposition in tensile properties of selective laser melted Ti-6Al-4V, *J. Alloy. Comp.* 744 (2018) 357–363.
- [16] E. Hernandez-Nava, C.J. Smith, F. Derguti, S. Tammas-Williams, F. Leonard, P.J. Withers, I. Todd, R. Goodall, The effect of defects on the mechanical response of Ti-6Al-4V cubic lattice structures fabricated by electron beam melting, *Acta Mater.* 108 (2016) 279–292.
- [17] P.A. Kobryn, S.L. Semiatin, The laser additive manufacture of Ti-6Al-4V, *J. Min. Met. Mat. Soc.* 53 (2001) 40–42.
- [18] M. Das, V.K. Balla, D. Basu, S. Bose, A. Bandyopadhyay, Laser processing of SiC-particle-reinforced coating on titanium, *Scripta Mat* 63 (2010) 438–441.
- [19] N.E. Hodge, R.M. Ferencz, J.M. Solberg, Implementation of a thermomechanical model for the simulation of selective laser melting, *Comp. Mech.* 54 (2014) 33–51.
- [20] W. Xu, E.W. Lui, A. Pateras, M. Qian, M. Brandt, In situ tailoring microstructure in additively manufactured Ti-6Al-4V for superior mechanical performance, *Acta Mater.* 125 (2017) 390–400.
- [21] J.J. Yang, J. Han, H.C. Yu, J. Yin, M. Gao, Z.M. Wang, X.Y. Zeng, Role of molten pool mode on formability, microstructure and mechanical properties of selective laser melted Ti-6Al-4V alloy, *Mat. Des.* 110 (2016) 558–570.
- [22] X.Y. Zhang, G. Fang, S. Leefang, A.J. Bottger, A.A. Zadpoor, J. Zhou, Effect of subtransus heat treatment on the microstructure and mechanical properties of additively manufactured Ti-6Al-4V alloy, *J. Alloy. Comp.* 735 (2018) 1562–1575.
- [23] M. Simonelli, Y.Y. Tse, C. Tuck, On the texture formation of selective laser melted Ti-6Al-4V, *Met. Mat. Trans. A Phys. Metallurgy* 45A (2014) 2863–2872.
- [24] H.Z. Zhong, X.Y. Zhang, S.X. Wang, J.F. Gu, Examination of the twinning activity in additively manufactured Ti-6Al-4V, *Mat. Des.* 144 (2018) 14–24.
- [25] E.W. Lui, W. Xu, A. Pateras, M. Qian, M. Brandt, New development in selective laser melting of Ti-6Al-4V: a wider processing window for the achievement of fully lamellar  $\alpha + \beta$  microstructures, *JOM* 69 (2017) 2679–2683.
- [26] P. Kürsteiner, M.B. Wilms, A. Weisheit, P. Barriobero-Vila, E.A. Jäggle, D. Raabe, Massive nanoprecipitation in an Fe-19Ni-xAl maraging steel triggered by the intrinsic heat treatment during laser metal deposition, *Acta Mater.* 129 (2017) 52–60.
- [27] S. Leuders, T. Lieneke, S. Lammers, T. Troster, T. Niendorf, On the fatigue properties of metals manufactured by selective laser melting - the role of ductility, *J. Mat. Res.* 29 (2014) 1911–1919.
- [28] G. Kasperovich, J. Hausmann, Improvement of fatigue resistance and ductility of TiAl6V4 processed by selective laser melting, *J. Mat. Proc. Tech.* 220 (2015) 202–214.
- [29] B. Vrancken, L. Thijs, J.P. Kruth, J. Van Humbeeck, Heat treatment of Ti6Al4V produced by selective laser melting: microstructure and mechanical properties, *J. Alloy. Comp.* 541 (2012) 177–185.
- [30] X.P. Tan, Y. Kok, W.Q. Toh, Y.J. Tan, M. Descroins, D. Manginck, S.B. Tor, K.F. Leong, C.K. Chua, Revealing martensitic transformation and alpha/beta interface evolution in electron beam melting three-dimensional-printed Ti-6Al-4V, *Sci. Rep.* 6 (2016) 26039.
- [31] N. Schell, A. King, F. Beckmann, T. Fischer, M. Muller, A. Schreyer, The high energy materials science beamline (HEMS) at PETRA III, in: H.G. Brokmeier, M. Muller, P.K. Pranzas, A. Schreyer, P. Staron (Eds.), *Mechanical Stress Evaluation by Neutrons and Synchrotron Radiation VI*, vol. 772, 2014, pp. 57–61.
- [32] A.P. Hammersley, S.O. Svensson, A. Thompson, Calibration and correction of spatial distortions in 2D detector systems, *Nuc. Instr. Met. Phys. Res. Sec.* 346 (1994) 312–321.
- [33] TOPAS, Version 6.0, Bruker AXS: Karlsruhe, Germany, 2015.
- [34] D.J. Larson, T.J. Prosa, R.M. Ullfig, B.P. Geiser, T.F. Kelly, *Local Electrode Atom Probe Tomography: a User's Guide*, Springer, New York, 2013.
- [35] K. Thompson, D. Lawrence, D.J. Larson, J.D. Olson, T.F. Kelly, B. Gorman, In situ site-specific specimen preparation for atom probe tomography, *Ultra-microscopy* 107 (2007) 131–139.
- [36] I. Gutierrez-Urrutia, C.L. Li, S. Emura, X.H. Min, K. Tsuchiya, Study of  $\{332\} < 113 >$  twinning in a multilayered Ti-10Mo-xFe ( $x = 1-3$ ) alloy by ECCI and EBSD, *Sci. Technol. Adv. Mater.* 17 (2016) 220–228.
- [37] J.W. Elmer, T.A. Palmer, S.S. Babu, E.D. Specht, In situ observations of lattice expansion and transformation rates of alpha and beta phases in Ti-6Al-4V, *Mat. Sci. Eng. A Struct. Mat.* 391 (2005) 104–113.
- [38] S. Malinow, W. Sha, Z. Guo, C.C. Tang, A.E. Long, Synchrotron X-ray diffraction study of the phase transformations in titanium alloys, *Mat. Char.* 48 (2002) 279–295.
- [39] Q.L. Huang, X.J. Liu, X. Yang, R.R. Zhang, Z.J. Shen, Q.L. Feng, Specific heat treatment of selective laser melted Ti-6Al-4V for biomedical applications, *Front. Mat. Sci.* 9 (2015) 373–381.

- [40] E.J. Mittemeijer, P. Scardi, *Diffraction Analysis of the Microstructure of Materials*, Springer-Verlag Berlin Heidelberg, 2004.
- [41] M.J. Donachie, *Titanium: A Technical Guide*, ASM International, ASM World Headquarters - Materials Park, Novelty, OH, 2000.
- [42] R. Boyer, G. Welsch, E.W. Collings, *Materials Properties Handbook: Titanium Alloys*, ASM International, ASM World Headquarters - Materials Park, Novelty, OH, 1994.
- [43] P. Barriobero-Vila, G. Requena, T. Buslaps, M. Alfeld, U. Boesenberg, Role of element partitioning on the  $\alpha$ - $\beta$  phase transformation kinetics of a bi-modal Ti-6Al-6V-2Sn alloy during continuous heating, *J. Alloy. Comp.* 626 (2015) 330–339.
- [44] R. Castro, L. Seraphin, *Mem. Sci. Rev. Metall.* 63 (1966) 1036.
- [45] R.W. Armstrong, Engineering science aspects of the Hall-Petch relation, *Acta Mech.* 225 (2014) 1013–1028.
- [46] D.C. Hofmann, S. Roberts, R. Otis, J. Kolodziejska, R.P. Dillon, J.O. Suh, A.A. Shapiro, Z.K. Liu, J.P. Borgonia, Developing gradient metal alloys through radial deposition additive manufacturing, *Sci. Rep.* 4 (2014) 5357.
- [47] H. Aboufadel, J. Deges, P. Choi, D. Raabe, Dynamic strain aging studied at the atomic scale, *Acta Mater.* 86 (2015) 34–42.
- [48] A. Kwiatkowski da Silva, G. Leyson, M. Kuzmina, D. Ponge, M. Herbig, S. Sandlöbes, B. Gault, J. Neugebauer, D. Raabe, Confined chemical and structural states at dislocations in Fe-9 wt.%Mn steels: a correlative TEM-atom probe study combined with multiscale modelling, *Acta Mater.* 124 (2017) 305–315.
- [49] M. Kuzmina, M. Herbig, D. Ponge, S. Sandlöbes, D. Raabe, Linear complexes: confined chemical and structural states at dislocations, *Science* 349 (2015) 1080–1083.